Environmental Science and Pollution Research (2023) 30:102446–102461
https://doi.org/10.1007/s11356-023-29475-9

RESEARCH ARTICLE

Natural phosphorus-ferromanganese ore-based composites for the simultaneous remediation of arsenic- and lead-co-contaminated groundwater: synergistic effectiveness, kinetics, and mechanisms

Hongli Lu[1,2] · Xiangjian Xu[2] · Yu Yang[2] · Han Xiao[2] · Fu Xia[2] · Xu Han[2] · Sheng Deng[2] · Shuxuan Wu[2] · Xingang Wang[2] · Yonghai Jiang[2] · Qinghua Yan[1]

Received: 9 March 2023 / Accepted: 19 August 2023 / Published online: 5 September 2023

Abstract

Natural phosphorus-ferromanganese ore (NPO-NFMO) based composites by mechanical ball milling method, applying for the simultaneous remediation of arsenic (As) and lead (Pb) co-contaminated groundwater. Kinetic behavior adopted pseudo-second-order adsorption mechanism attaining equilibrium in 120 min over a wide pH range (2.0–6.0). NPO-NFMO realized higher adsorption capacity for As(III) (6.8 mg g^{-1}) and Pb(II) (26.5 mg g^{-1}) than those of single NPO (1.7 and 7.8 mg g^{-1}) and NFMO (2.9 and 5.1 mg g^{-1}), indicating that synergistic effects of NPO and NFMO considerably enhanced the adsorption capacity in mixed adsorption system. Fresh and used NPO-NFMO were characterized, and indicated that NPO-NFMO formed stable minerals of $PbAs_2O_6$ and $PbFe_2(AsO_4)_2(OH)_2$. The underlying adsorption mechanism indicated that As(III) and Pb(II) removal was involved with multiple mechanisms, including electrostatic adsorption, oxidation, complexation, and coprecipitation. The effects of key reaction parameters including mass ratios of NPO and NFMO, initial metal ion concentration, dosage, solution pH, and co-existing anions in groundwater were systematically investigated. The novel designed NPO-NFMO-based composites can be deemed as a promising amendment for simultaneous immobilization of As(III) and Pb(II) in co-contaminated soil and groundwater.

Keywords Phosphorus-ferromanganese ore-based composites · Arsenic- and lead-co-contaminated groundwater · Effectiveness · Kinetics · Mechanisms

Introduction

Heavy metals are common pollutants in contaminated soil and groundwater, which are considered highly toxic and difficult to degrade, resulting in remediation of heavy-metal-contaminated groundwater being recognized as an important issue so far. Arsenic (As) and lead (Pb) were ubiquitous environmental toxins, and ranked 1st and 2nd in the United States Agency for Toxic Substances and Disease Registry 2019 Priority Lis t (Shi et al. 2021). The dominant states of As in groundwater were As(III) and As(V), while As(III) is 60 times more toxic than As(V) (Jain and Ali 2000). Long-term exposure to Pb can cause Pb poisoning and neurological disorders (Bhaumik et al. 2021). It is noteworthy that As and Pb contamination often co-exist and are more active and toxic than each single element. Hence, the remediation of As and Pb co-contaminated soil and groundwater is imperative (Wang et al. 2019; Xia et al. 2017).

Responsible Editor: Ioannis A. Katsoyiannis

Hongli Lu and Xiangjian Xu contributed equally to this work.

Responsible Editor: Ioannis A. Katsoyiannis.

✉ Yonghai Jiang
jyhai203@126.com

[1] Qingdao Engineering Research Center for Rural Environment, College of Resources and Environment, Qingdao Agricultural University, Qingdao 266109, People's Republic of China

[2] State Key Laboratory of Environmental Criteria and Risk Assessment and State Environmental Protection Key Laboratory of Simulation and Control of Groundwater Pollution, Chinese Research Academy of Environmental Sciences, Beijing 100012, People's Republic of China

Among the various remediation techniques including adsorption, coagulation, flocculation, ion exchange, electrodialysis, and membrane separation, adsorption was most frequently used owing to its straightforward, operational simplicity, high efficiency, and cost effectiveness (Meng et al. 2019). To date, diverse passivation agents, such as iron-manganese-based materials (Qureshi et al. 2022), phosphorus-based materials(Cui et al. 2022), and biocarbon materials (Liao et al. 2022) have been widely used for heavy metal adsorption, which exhibited superior performance owing to the large surface areas and preferred surface properties. Recent researches focus on investigation of cost-efficient sorbents and the use of adsorbents based on natural waste, and other readily available materials to develop low-cost treatment strategies.

In many natural mineral materials, iron-based materials are widely evaluated owing to their magnetic properties, many active sites and high activity (Akin et al. 2012; Sun et al. 2019; Zhang et al. 2007). However, most studies have shown that iron-based materials exhibit better removal performance for As(V) than As(III) (Cheng et al. 2016) mainly because of the low affinity for arsenite (AsO_2^-) at low concentrations of adsorbent, which requires an oxidative pretreatment to improve removal performance (Chen et al. 2018; Zhang et al. 2020). Considering the high oxidation potential of manganese oxides for As(III), it is an effective additive for iron-based oxides, improving their adsorption capacity toward As(III) in a wide pH range including acidic environment (Gude et al. 2017; Lenoble et al. 2004; Wang et al. 2020). Thus, an environmentally friendly natural ferromanganese ore (NFMO) is very advantageous for the removal of As-containing pollutants. In addition, natural phosphate ore (NPO, $Ca_5(PO_4)_3F$) has been proven to be another efficient and promising amendment due to low cost, water insolubility, high biocompatibility, and high capacity toward heavy metals. Note that Ca^{2+} in NPO can be replaced with metal cations such as Pb^{2+} via ion exchange reactions, resulting in excellent cation adsorption. NPO can combine with Pb^{2+} to form stable precipitates, effectively slowing down the migration and transformation ability, reducing their biological toxicity. However, these natural mineral materials still suffer from low capacity in the mixture of heavy metals anions and cations ions removal. The main objective of heavy metal adsorption was to remove a single or the same kind of heavy metal. Previous research of simultaneous or selective removal of multi-component heavy metals was limited, leading to a negative effect on remediation of heavy metals co-contaminated sites. Therefore, in view of the completely opposite chemical properties of Pb-As and the difficulty of simultaneous detoxification, it is of great significance to develop the natural mineral based composites for the simultaneous effectively remediation of arsenic-and lead-co-contaminated soil and groundwater.

Herein, the main objectives of the present study were to develop a novel natural phosphorus-ferromanganese ore (NPO-NFMO) based composites and systematically investigate the potential synergistic effects for the simultaneous remediation of arsenic- and lead-co-contaminated groundwater. The mechanism of As(III) and Pb(II) removal were proposed by the characteristics of the changes in physicochemical properties of natural phosphorus-ferromanganese ore-based composites before and after reaction. Furthermore, the effect of key reaction parameters including mass ratios of NPO and NFMO, initial dosage, and pH was also explored and the effect of co-existing anions in groundwater on the simultaneous removal of As(III) and Pb(II) by NPO-NFMO composites were systematically investigated.

Materials and methods

Materials

All solutions were prepared with ultrapure deionized water (18.2 MΩ cm^{-1}, Millipore). The multi-metal stock solution was prepared with ultrapure deionized water using sodium arsenite and lead nitrate, which were purchased from the Sinopharm Group Chemical Reagent Co., Ltd. All reagents were of analytical grade without further treatment.

Preparation of the NPO-NFMO-based composites

Natural phosphorus ores (NPO) were purchased in Chaoyang City, Liaoning Province, China. Natural ferromanganese ores (NFMO) were obtained from Gabon, South Africa. These natural minerals were first ground by ball mill, screened for 100 meshes and set aside. The chemical composition of selected natural minerals was analyzed by X-ray fluorescence (XRF, AB104L, AxiosmAX) and the results were shown in Table S1 and S2 in Supplementary Materials (SM).

The NPO-NFMO-based composites with different mass ratios of NPO and NFMO (NPO: NFMO = 1:1, 1:2, 1:3, 1:4, 4:1, 3:1, and 2:1) were synthesized by the modified methods reported before via mechanical ball milling method according to the following procedure (Gao et al. 2015; Li et al. 2009). Various proportions of NPO and NFMO mass were weighed, and then added to two ball milling tanks and sealed. Before ball milling, high-purity argon gas was filled to protect the samples during ball milling. The spheroink tank was made of stainless steel, lined with PTFE tank, and the grinding ball was grinding with four kinds of zirconia ball, with a mass ratio of 3:8:20:8 and a ball-to-material ratio of 35:1. The NPO-NFMO-based composites with different mass ratios of NPO and NFMO were prepared by alternating forward ball milling (550 rpm) for 10 min, followed reverse ball milling (550 rpm) for 10 min, so that

the cumulative ball milling time of the mixture of NPO and NFMO reached 8 h. All as-prepared powders were abbreviated as 1NPO-1NFMO, 1NPO-2NFMO, 1NPO-3NFMO, 1NPO-4NFMO, 4NPO-1NFMO, 3NPO-1NFMO, and 2NPO-1NFMO, which were representative of different mass ratios of NPO and NFMO as 1:1, 1:2, 1:3, 1:4, 4:1, 3:1, and 2:1, respectively.

Adsorption kinetics experiments

The adsorption efficiency of As(III) and Pb(II) on the NPO-NFMO composites were obtained using batch tests at pH = 6.0. Then, 150 mg of the NPO-NFMO composite with the mass ratio of 1:4 was loaded in the 100 mL Erlenmeyer flasks. Initial As(III) and Pb(II) concentrations were 5 mg L^{-1} and 15 mg L^{-1}, respectively. The Erlenmeyer flasks were placed on the horizontal oscillator at 160 rpm for 120 min at 25 ± 1 ℃. Simultaneously, series of batch tests were performed to investigate the effect of NPO-NFMO composites with the different mass ratio (1:1, 1:2, 1:3, 1:4, 2:1, 3:1, and 4:1), dosage (0.5, 1, 1.5, 2, and 3 g L^{-1}), initial pH (2, 3, 4, and 6), initial combined contamination concentrations (As(III) 2 mg L^{-1} + Pb(II) 6 mg L^{-1}, As(III) 5 mg L^{-1} + Pb(II) 15 mg L^{-1}, and As(III) 10 mg L^{-1} + Pb(II) 30 mg L^{-1}) and coexisting anion (SO_4^{2-} and Cl^-) on the adsorption efficiency. The pH was adjusted to 2, 3, 4, and 6 with dilute HNO_3 and/or NaOH solution to avoid the metal precipitation caused by hydrolysis at pH > 6. The changes of As(III), As(V), and Pb(II) concentration in the treated solutions were analyzed after time intervals (0, 5, 20, 40, 60, and 120 min) by using inductively coupled plasma-mass spectrometry (ICP-MS, Agilent 7800, U.S.A) and liquid chromatography-atomic fluorescence spectroscope (LC-AFS, Haiguang 6500, China).

Kinetics experiments were conducted in batches to determine the adsorption efficiency of As(III) and Pb(II) from arsenic- and lead-co-contaminated groundwater onto the NPO-NFMO composite. Two adsorption kinetics models (pseudo-first-order kinetic model Eq. (1) and pseudo-second-order kinetic model Eq. (2)) were analyzed to evaluate the experiment data. The arsenic and lead adsorption capacity on NPO-NFMO composite was calculated using the following equation:

$$q_t = q_e \times \left(1 - e^{-k_1 t}\right) \tag{1}$$

$$\frac{t}{q_t} = \frac{1}{k_2 q_e^2} + \frac{t}{q_e} \tag{2}$$

$$q_e = \frac{V \times (C_0 - C_t)}{m} \tag{3}$$

where q_e (mg g^{-1}) was the removal amount of the NPO-NFMO base composite at the equilibrium concentration (Eq. (3)), q_t was the amounts of subjected analyte adsorbed (mg g^{-1}) at any time (min). k_1 (min^{-1}) and k_2 (g mg^{-1} min^{-1}) are the rate constant of the pseudo-first-order kinetic model and pseudo-second-order kinetic model, respectively. V (L) represented the solution volume. m (g) meant mass of the NPO-NFMO composites. C_t (mg L^{-1}) and C_0 (mg L^{-1}) are the equilibrium combined contamination concentrations and initial combined contamination concentration, respectively.

Analytical and characterization methods

The surface morphologies of NPO, NFMO, and NPO-NFMO composites were analyzed by scanning electron microscopy (SEM, SU-8010, Hitachi) and the elements compositions were detected by energy dispersive X-Ray spectrometer (EDS) and elemental mapping analysis. The zeta potential measurements were tested on a Malvern Zetasizer NanoZSP (Malvern Instruments Ltd, UK). The crystallinity and chemical composition of the sample powder were identified by X-ray powder diffraction (XRD) analysis with Cu Kα radiation in the range of 10–80° (Bruker D8 advance Germany). Fourier transform infrared spectroscope (FT-IR, Tensor II, Bruker, Germany) was used to identify the distribution of functional groups on the sample surface between different materials at a resolution of 1 cm^{-1}. X-ray photoelectron spectroscopy (XPS) was used to analyze the elemental chemical states and surface composition in composites materials before and after adsorption process. Zero point charge pH (pH_{ZPC}) of the NPO-NFMO composite was determined by acid–base titration method as described by Stumm and Morgan (Stumm and Morgan 1996). The specific surface area and pore size of adsorbents material was measured by Brunauer–Emmett–Teller (BET) N_2 adsorption method where the samples were dried with a constant flow of N_2 at 60 ℃ for 24 h (ASAP 2460, McMortic, USA).

Results and discussion

Characterization of the NPO-NFMO-based composites

The phase and crystallinity information of the fresh NPO, NFMO, and NPO-NFMO-based composites characterized by XRD measurement were shown in Fig. 1. The characteristic peaks of the fresh NPO were clearly observed at 2θ = 31.9°, 32.3°, 33.1°, and 34.1°. These peaks matched well with the JCPDS data for $Ca_5(PO_4)_3F$ (JCPDS No. 15–0876) (Zhang et al. 2014). The fresh NFMO contained complex composition and weak crystallinity due to the peaks with wide and low intensity. The characteristic peaks of the fresh NFMO were clearly observed at 2θ = 21.2°, 26.3°, and 36.6°, which matched well with the JCPDS data for goethite (FeOOH) (JCPDS No. 29–0713) (Hu et al. 2019) and MnO_2 (JCPDS

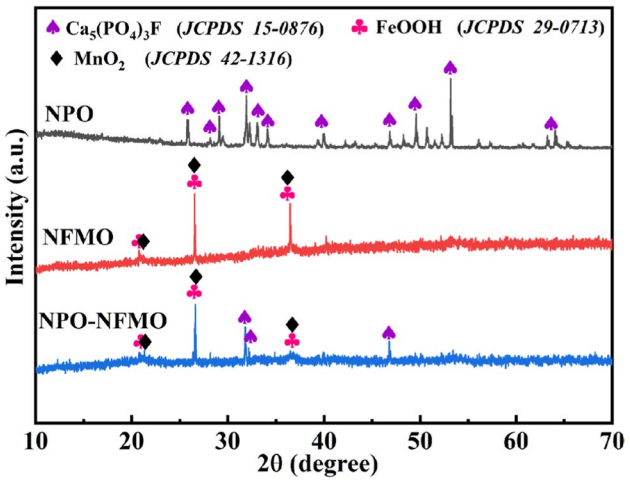

Fig. 1 XRD patterns of the fresh NPO, NFMO, and NPO-NFMO-based composites

No.42–1316) (Feng et al. 2020). The characteristic peaks of the fresh NPO-NFMO-based composites matched well with the JCPDS data for $Ca_5(PO_4)_3F$ (JCPDS No.15–0876), MnO_2 (JCPDS No.42–1316), and FeOOH (JCPDS No.29–0713), indicating that the two minerals were thoroughly mixed together.

To understand surface morphologies of the fresh NPO, NFMO, and NPO-NFMO composite, SEM analysis were performed. As shown in Fig. 2, fresh NPO was more dispersed and has larger particles. By contrast, the NFMO particles had a cluster structure and possessed a certain specific saturation magnetization of 2.38 emu g^{-1} (Fig. S1). The NPO-NFMO-based composite exhibited sheet-like particles with a cluster structure. The specific saturation magnetization of the NPO-NFMO-based composite decreased to 1.80 emu g^{-1}. The calculated BET specific surface areas for the fresh NPO, NFMO, and NPO-NFMO composite were 10.39, 148.98, and 97.98 $m^2 g^{-1}$, respectively. NPO particles displayed a size distribution around 2.6 μm; while NFMO was at around 1.3 μm. In a similar trend to the surface area results measured by BET, NPO-NFMO had a smaller particle size than NPO due to the successful loading of NFMO, but was larger than NFMO at 1.5 (Fig. S2). Therefore, the surface area of NPO-NFMO composite material increased, indicating an increase in its reactivity.

Synergistic effectiveness and kinetics

Figure 3 showed the synergistic removal efficiency of As(III) and Pb(II) by the NPO-NFMO-based composites. The removal efficiencies of NPO, NFMO, and NPO-NFMO-based composite were compared. The removal efficiencies

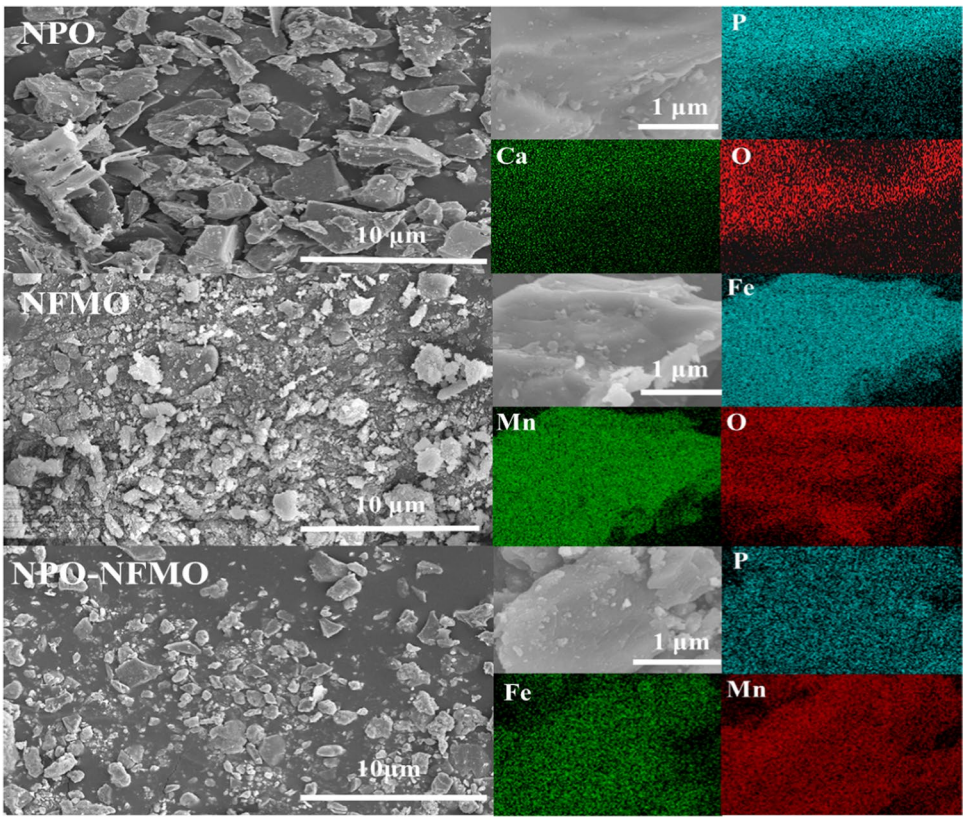

Fig. 2 SEM images and EDS-mapping of the fresh NPO, NFMO and NPO-NFMO

of As(III) + Pb(II) by NPO, NFMO, and NPO-NFMO-based composite were 44.2 + 58.8%, 99.8 + 32.4%, and 100 + 100% after 120 min. A much higher removal efficiency of As(III) and Pb(II) concentration was observed in the presence of NPO-NFMO-based composite, suggesting that the synergistic contribution between NPO and NFMO was non-negligible. NPO-NFMO realized higher adsorption capacity for As(III) (3.1 mg g^{-1}) and Pb(II) (12.5 mg g^{-1}) than those of either NPO (1.3 mg g^{-1} and 7.3 mg g^{-1}) or NFMO (2.7 mg g^{-1} and 4.1 mg g^{-1}). After finally determining the best ratio of NPO-NFMO materials, it was compared with two common types of materials on the market, Hematite and Manganese, respectively (Fig. S3). The results showed that NPO-NFMO has good removal performance of As(III) and Pb(II) composite pollution. We also performed the dissolution of metal ion from the NPO-NFMO (Fig. S4). It showed that after 120 min of adsorption, the leaching concentration of Fe, Mn, and P are lower than those before adsorption, and lower than the groundwater quality standard. It indicates that the NPO-NFMO material can be studied extensively as a restoration material.

The pseudo-first-order and pseudo-second-order were used to describe kinetic mechanism of the adsorption process (Fig. 4a, b). As observed, the regression coefficients of the pseudo-second order kinetic fitting (Fig. 4b) for the NPO, NFMO and NPO-NFMO-based composite are greater than that of the pseudo-first-order kinetic fitting (Fig. 4a), indicating that the adsorption reaction was more consistent with the pseudo-second-order kinetic model. Specifically, the As(III) and Pb(II) removal rate constant of the pseudo-second-order kinetic model onto NPO-NFMO-based composite were 1.1×10^{-1} g mg^{-1} min^{-1} and 7.2×10^{-2} g mg^{-1} min^{-1}, respectively, which were observably higher than those of either NPO (4.7×10^{-2} g mg^{-1} min^{-1} and 1.5×10^{-2} g mg^{-1} min^{-1}) or NFMO (5.4×10^{-2} g mg^{-1} min^{-1} and 1.3×10^{-2} g mg^{-1} min^{-1}). The adsorption of As(III) and Pb(II) by NPO-NFMO-based composite was likely to be kinetically controlled as a second-order reaction and this adsorption was dependent on the concentration of both adsorbent and adsorbate. Figure S5 showed the potential energy of NPO-NFMO before and after adsorption. After adsorption, the Zero point charge pH (pH_{ZPC}) of NPO-NFMO moved from 5.1 to 6.25. The results revealed that chemisorption was the main adsorption mechanism, involving electrostatic attraction (Ain et al. 2020).

Effect of mass ratios of NPO and NFMO, initial dosage, and pH

Figure 5a, b showed the synergistic removal efficiency of NPO-NFMO composites for As(III) and Pb(II) with different ratios. After 120 min, 1NPO-4NFMO showed the highest removal rate for As(III) + Pb(II). The pseudo-second-order kinetic model analysis of the adsorption data of As(III) and Pb(II) onto the NPO-NFMO-based composites with different mass ratios. It can be observed that the As(III) removal rate constant of the pseudo-second order kinetic model increased from 2.0×10^{-2} g mg^{-1} min^{-1} (1NPO-1NFMO) and 1.9×10^{-2} g mg^{-1} min^{-1} (1NPO-2NFMO) to 4.8×10^{-2} g mg^{-1} min^{-1} (1NPO-3NFMO) and 1.05×10^{-1} g mg^{-1} min^{-1} (1NPO-4NFMO), and then decreased to 1.6×10^{-2} g mg^{-1} min^{-1} (2NPO-1NFMO), 1.6×10^{-2} g mg^{-1} min^{-1} (3NPO-1NFMO), and 2.0×10^{-2} g mg^{-1} min^{-1} (4NPO-1NFMO). Similarly, the Pb(II) removal rate constant decreased from 1.2×10^{-2} g mg^{-1} min^{-1} (1NPO-1NFMO) to 1.1×10^{-2} g mg^{-1} min^{-1} (1NPO-2NFMO), and 1.1×10^{-2} g mg^{-1} min^{-1} (1NPO-3NFMO), and then abruptly increased to 7.2×10^{-2} g mg^{-1} min^{-1} (1NPO-4NFMO), and finally decreased to 1.1×10^{-2} g mg^{-1} min^{-1} (2NPO-1NFMO), 2.0×10^{-2} g mg^{-1} min^{-1} (3NPO-1NFMO), and 1.7×10^{-2} g mg^{-1} min^{-1} (4NPO-1NFMO). Results indicated that the mass ratio within a certain range could enhance the synergistic contribution from NPO and NFMO. Therefore, 1NPO-4NFMO was chosen to better elucidate NPO-NFMO in the removal of the combined As(III) and Pb(II).

The NPO-NFMO-based composite dose plays a significant role in the optimization of adsorption capacity. The effect of the NPO-NFMO-based composite dose was examined by adding 0.5, 1, 1.5, 2, and 3 g L^{-1} of 1NPO-4NFMO

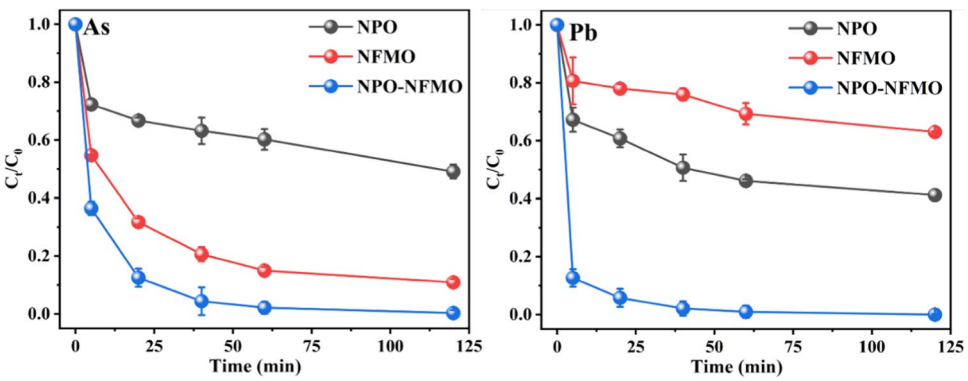

Fig. 3 Synergistic removal efficiency of As(III) and Pb(II) by NPO, NFMO, and NPO-NFMO-based composite. Reaction conditions: [As(III)] = 5 mg L^{-1}, [Pb(II)] = 15 mg L^{-1}, adsorbents dosage of 1.5 g L^{-1}, V = 100 mL

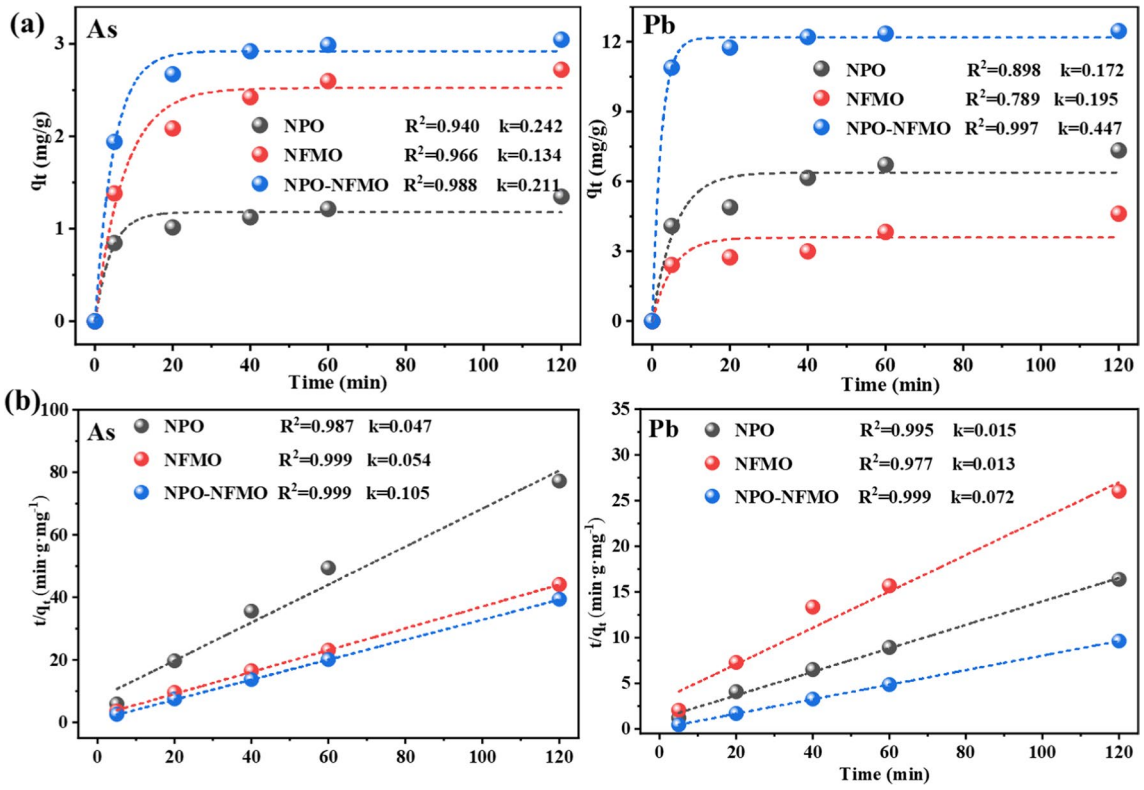

Fig. 4 Pseudo-first-order (**a**) and pseudo-second-order (**b**) kinetic model analysis of the adsorption data of As(III) and Pb(II) onto the NPO, NFMO, and NPO-NFMO based composite

to 100 mL of 5 mg L^{-1} As(III) and 15 mg L^{-1} Pb(II) aqueous solution and shaking for 120 min. Figure 6 showed the synergistic removal efficiency of NPO-NFMO composites, pseudo-second-order kinetic model analysis of the adsorption data of As(III) and Pb(II) onto the 1NPO-4NFMO-based composite. It was observed that the As(III) removal rate constant increased from 1.3×10^{-2} g mg^{-1} min^{-1} to 2.1×10^{-2} g mg^{-1} min^{-1}, 1.1×10^{-1} g mg^{-1} min^{-1}, 1.2×10^{-1} g mg^{-1} min^{-1}, and 2.4×10^{-1} g mg^{-1} min^{-1} with an increase in adsorbent dose due to the increase in the availability of more adsorption sites occupying the adsorbate. However, the Pb(II) removal rate constant first increased from 1.0×10^{-2} g mg^{-1} min^{-1} to 1.2×10^{-2} g mg^{-1} min^{-1} and 7.2×10^{-2} g mg^{-1} min^{-1}, and then decreased to 1.3×10^{-2} g mg^{-1} min^{-1} and 2.8×10^{-2} g mg^{-1} min^{-1}. This might be attributed to the adsorption sites of As(III) and Pb(II) increased with the increase amount of 1NPO-4NFMO, but when the amount of 1NPO-4NFMO was excessive, the utilization rate of adsorption sites reduced and the adsorption capacity decreased due to overlap of adsorption sites. In addition, the produced As(V) in solution was detected during 1NPO-4NFMO reacting with As(III). Figure 6c also showed that the residual As(V) concentrations in solution were very low, suggesting most of As(V) produced by As(III) oxidation could be subsequently adsorbed by 1NPO-4NFMO. The decrease of As(V) was far more quickly than the decrease of As(III). Combined with kinetic modeling, As(III) removal was mainly oxidation followed by chemical reactions. Fe in the NPO-NFMO was more likely to react preferentially with As(V) to form low-solubility substances, so co-precipitation may be one of the main mechanisms for As(V) adsorption (Bhowmick et al. 2014).

The pH value was an important index of adsorption experiment research, in order to further explore the influence of pH on adsorption capacity, the influence of pH (in the range of 2.0–6.0) on As(III) and Pb(II) removal efficiency of 1NPO-4NFMO was explored. As shown in Fig. 7, with the increase of pH (2.0–6.0), the removal rate constant of As(III) increased gradually from 6.3×10^{-2} g mg^{-1} min^{-1} (pH = 2) and 5.6×10^{-2} g mg^{-1} min^{-1} (pH = 3) to 1.0×10^{-1} g mg^{-1} min^{-1} (pH = 4) and 1.1×10^{-1} g mg^{-1} min^{-1} (pH = 6). The surface potential of the NPO-NFMO composite at experimental pH (1.0–6.0) was − 3–5.87 mV (Fig. S5), so the electrostatic adsorption could partially explain their effective immobilization for As(III). Similarly, the removal rate constant of Pb(II)

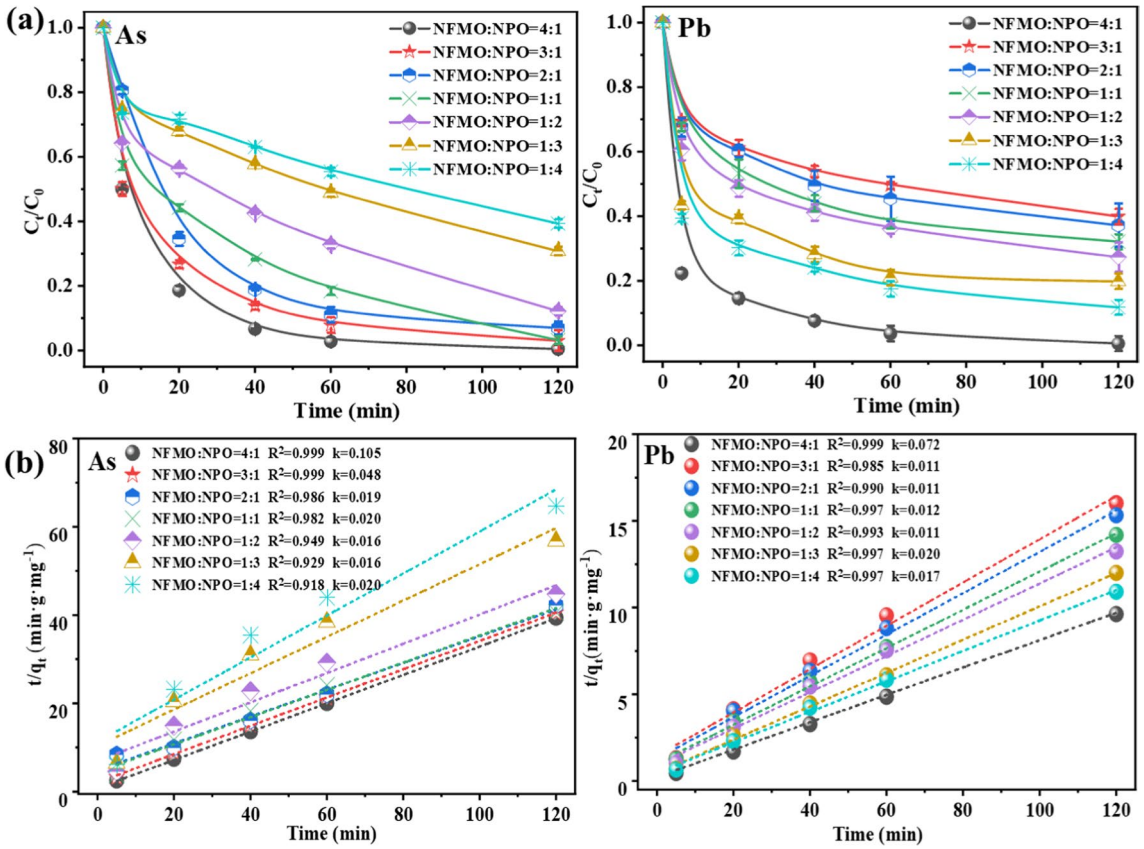

Fig. 5 Synergistic removal efficiency of As(III) and Pb(II) onto the NPO-NFMO-based composites with different mass ratios (**a**) pseudo-second-order kinetic model (**b**). Reaction conditions: [As(III)] = 5 mg L^{-1}, [Pb(II)] = 15 mg L^{-1}, the NPO-NFMO-based composites dosage with a mass ratio of 1:1, 1:2, 1:3, 1:4, 4:1, 3:1, and 2:1 of 1.5 g L^{-1}, V = 100 mL

increased gradually from 5.0×10^{-3} g mg^{-1} min^{-1} (pH = 2) to 1.7×10^{-2} g mg^{-1} min^{-1} (pH = 3), 1.1×10^{-1} g mg^{-1} min^{-1} (pH = 4), and 7.2×10^{-2} g mg^{-1} min^{-1} (pH = 6). When the initial pH was 2.0, Pb(II) and H^+ competed for adsorption sites on the adsorbent surface, and the removal rates of 1NPO-4NFMO was low. However, with the increase of pH value, the concentration of H^+ in the solution decreased, thus increasing the adsorption site of Pb(II) on the surface of the adsorbent. When pH was 4.0, the removal efficiency of Pb(II) increased a lot, which was on account of the preponderance of Pb^{2+} in the solution. The adsorption efficiency of Pb(II) decreased when pH = 6.0. The pH value of the solution will affect the existence form of Pb(II). At low pH value, the reason for less Pb(II) adsorption was that Pb(II) and H^+ competed for adsorption sites (Wang et al. 2022). As observed in Fig. 7, the residual As(V) concentrations in solution were very low, suggesting most of As(V) produced by As(III) oxidation could be subsequently adsorbed by 1NPO-4NFMO.

Effect of initial arsenic- and lead-co-contaminated concentrations and coexisting anion

As showed in Fig. 8, with the increase of the initial concentration of complex pollutants, the removal efficiency of As(III) and Pb(II) by NPO-NFMO decreased, corresponding the removal rate constant of As(III) decreased gradually from 3.9×10^{-1} g mg^{-1} min^{-1} to 1.1×10^{-1} g mg^{-1} min^{-1} and 2.0×10^{-2} g mg^{-1} min^{-1} and the removal rate constant of Pb(II) decreased from 5.2×10^{-1} g mg^{-1} min^{-1} to 7.2×10^{-2} g mg^{-1} min^{-1} and 1.3×10^{-2} g mg^{-1} min^{-1}. When the adsorbent was 1.5 g L^{-1}, the adsorption sites on the surface of the adsorbent was fixed, with the increase of the initial concentration of As(III) and Pb(II), the adsorption sites was gradually occupied. When the initial concentration of As(III) and Pb(II) was 10 mg L^{-1} and 30 mg L^{-1}, the adsorption capacity was the highest. The maximum removal of As(III) was 6.8 mg g^{-1} at an initial concentration of 10 mg L^{-1}, while maximum removal of Pb(II) was

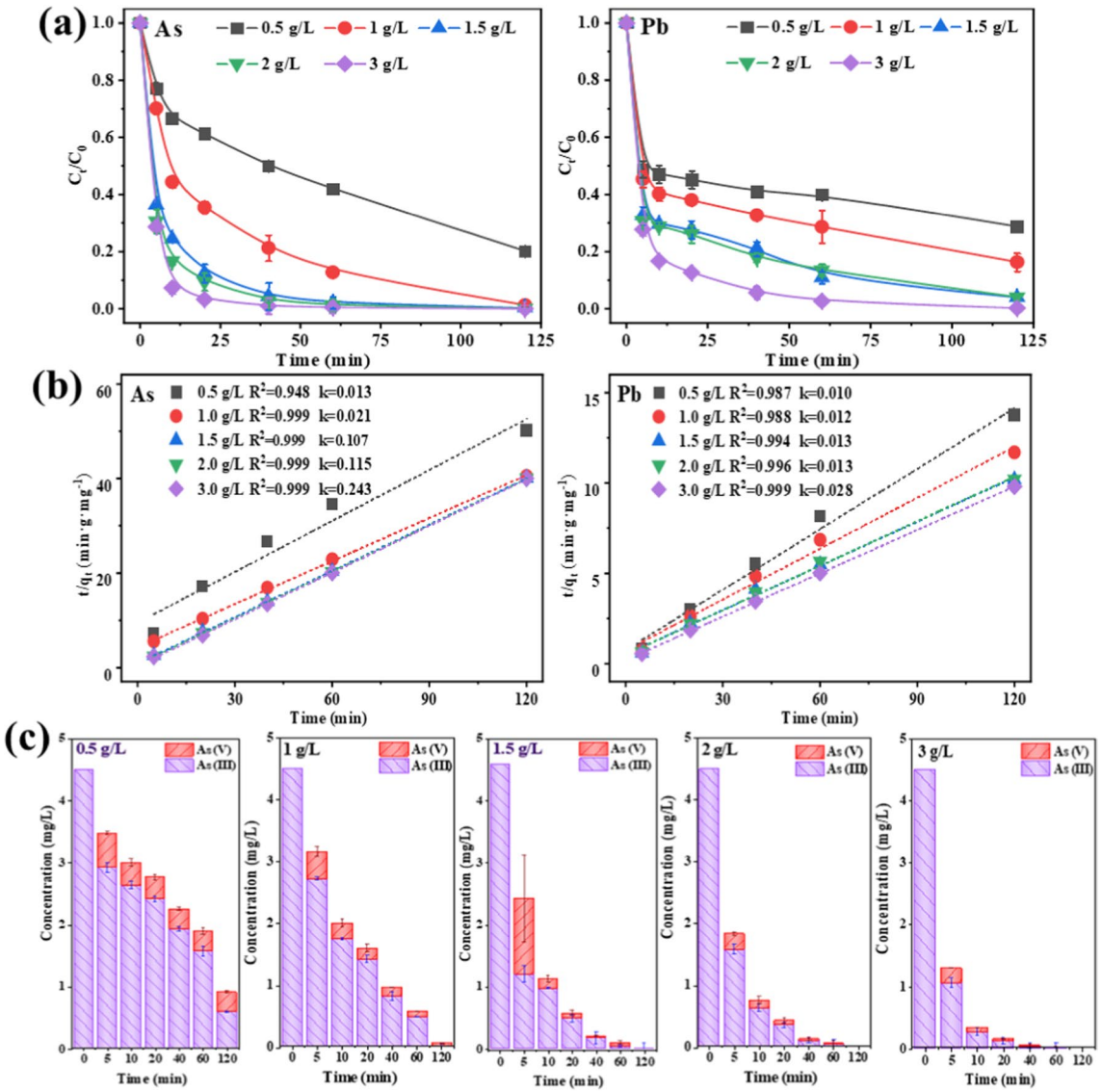

Fig. 6 Synergistic removal efficiency of As(III) and Pb(II) by NPO-NFMO-based composite with different initial dosages (**a**), pseudo-second-order kinetic model (**b**) and variation in the residual concentration of As(III) and As(V) (**c**). Reaction conditions: [As(III)] = 5 mg L^{-1}, [Pb(II)] = 15 mg L^{-1}, 1NPO-4NFMO-based composite dosage of 0.5, 1, 1.5, 2, and 3 g L^{-1}, V = 100 mL

achieved at the initial concentration of 30 mg L^{-1} with an equilibrium removal of 26.5 mg g^{-1}. When the initial concentration of As(III) and Pb(II) continued to increase, the adsorption capacity reached adsorption equilibrium. As observed in Fig. 8, the residual As(V) concentrations in solution were also very low, suggesting most of As(V) produced by As(III) oxidation could be subsequently adsorbed by 1NPO-4NFMO.

Figure 9 showed the synergistic removal efficiency of As(III) and Pb(II) by NPO-NFMO with co-existing anions in groundwater and pseudo-second-order kinetic model analysis of the adsorption data of As(III) and Pb(II) by 1NPO-4NFMO-based composite with co-existing anions (SO_4^{2-} and Cl^-) in groundwater. SO_4^{2-} and Cl^- were selected because they are abundant in natural groundwater and interfere in As(III) and Pb(II) removal. Results showed that the removal rate constant of As(III) and Pb(II) were significantly influenced by an increase in coexisting anions concentrations. With the increase of the initial SO_4^{2-} concentration from 1 mmol L^{-1} to 10 mmol L^{-1}, the removal rate constant of As(III) was suppressed, decreasing sharply from 1.1×10^{-1} g mg^{-1} min^{-1} (CK) to 2.9×10^{-2} g mg^{-1} min^{-1}, 3.2×10^{-2} g mg^{-1} min^{-1}, and 3.6×10^{-2} g mg^{-1} min^{-1}. However, the removal rate constant of As(III) barely changed with the increase of the initial Cl^- concentration from 1 to 20 mmol L^{-1}. Meanwhile, the concentration changes of high concentration SO_4^{2-} initial and post-reaction were detected, it was clear that the concentration decreased by 22.9% after 120 min of co-existing reaction

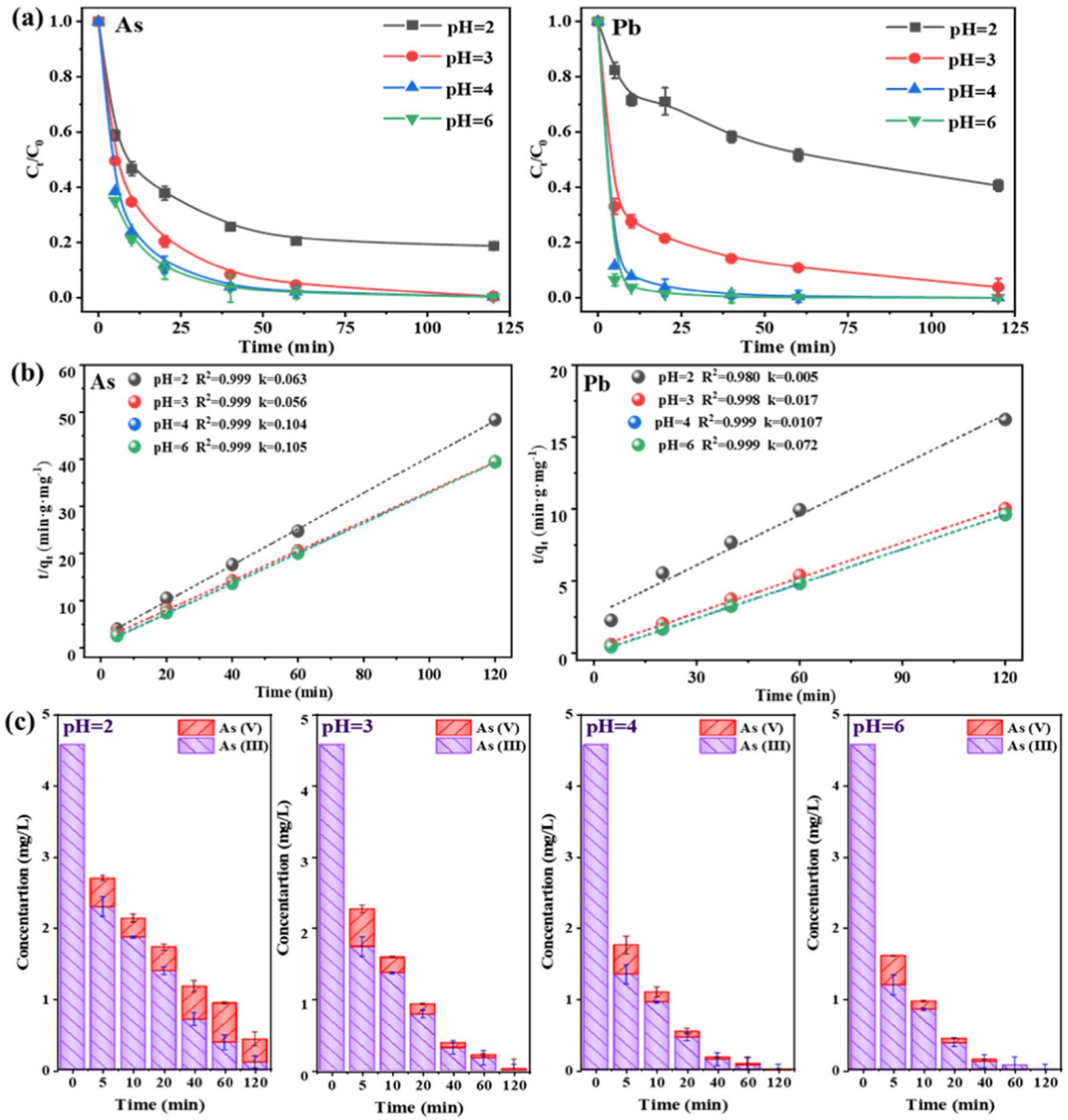

Fig. 7 Synergistic removal efficiency of As(III) and Pb(II) by NPO-NFMO with different initial pH (**a**), pseudo-second-order kinetic model analysis (**b**), and variation in the residual concentration of As(III) and As(V) (**c**). Reaction conditions: [As(III)] = 5 mg L^{-1}, [Pb(II)] = 15 mg L^{-1}, 1NPO-4NFMO-based composite dosage of 1.5 g L^{-1}, initial pH 2.0, 3.0, 4.0, and 6.0, V = 100 mL

(Fig. S6). These might be attributed to competitive adsorption between SO_4^{2-} and As(III) for the adsorption sites on the surface of 1NPO-4NFMO-based composite (Guan et al. 2009). Similarly, with the increase of the initial SO_4^{2-} concentration from 1 to 10 mmol L^{-1}, the removal rate constant of Pb(II) first decreased from 7.2×10^{-2} g mg^{-1} min^{-1} (CK) to 9.0×10^{-3} g mg^{-1} min^{-1}, and then increased to 3.5×10^{-2} g mg^{-1} min^{-1} and 4.2×10^{-2} g mg^{-1} min^{-1}. The removal rate constant of Pb(II) first decreased from 7.2×10^{-2} g mg^{-1} min^{-1} (CK) to 8.0×10^{-3} g mg^{-1} min^{-1}, and then increased to 2.1×10^{-2} g mg^{-1} min^{-1} and 2.5×10^{-2} g mg^{-1} min^{-1} with the increase of the initial Cl^- concentration from 1 to 20 mmol L^{-1}. These might be attributed to substitution and dissolution–precipitation reactions could result in the formation of chlorapatite ($Ca_5(PO_4)_3Cl$), chloropyromorphite ($Pb_5(PO_4)_3Cl$), $Ca_5(PO_4, SO_4)_3OH$ and $Pb_5(PO_4, SO_4)_3OH$ (Ma et al. 1994).

Synergistic mechanisms for the NPO-NFMO-based composites

In order to clarify the synergistic adsorption mechanisms of the NPO-NFMO-based composite, the composite after reaction was collected and analyzed. Figure 10a showed that

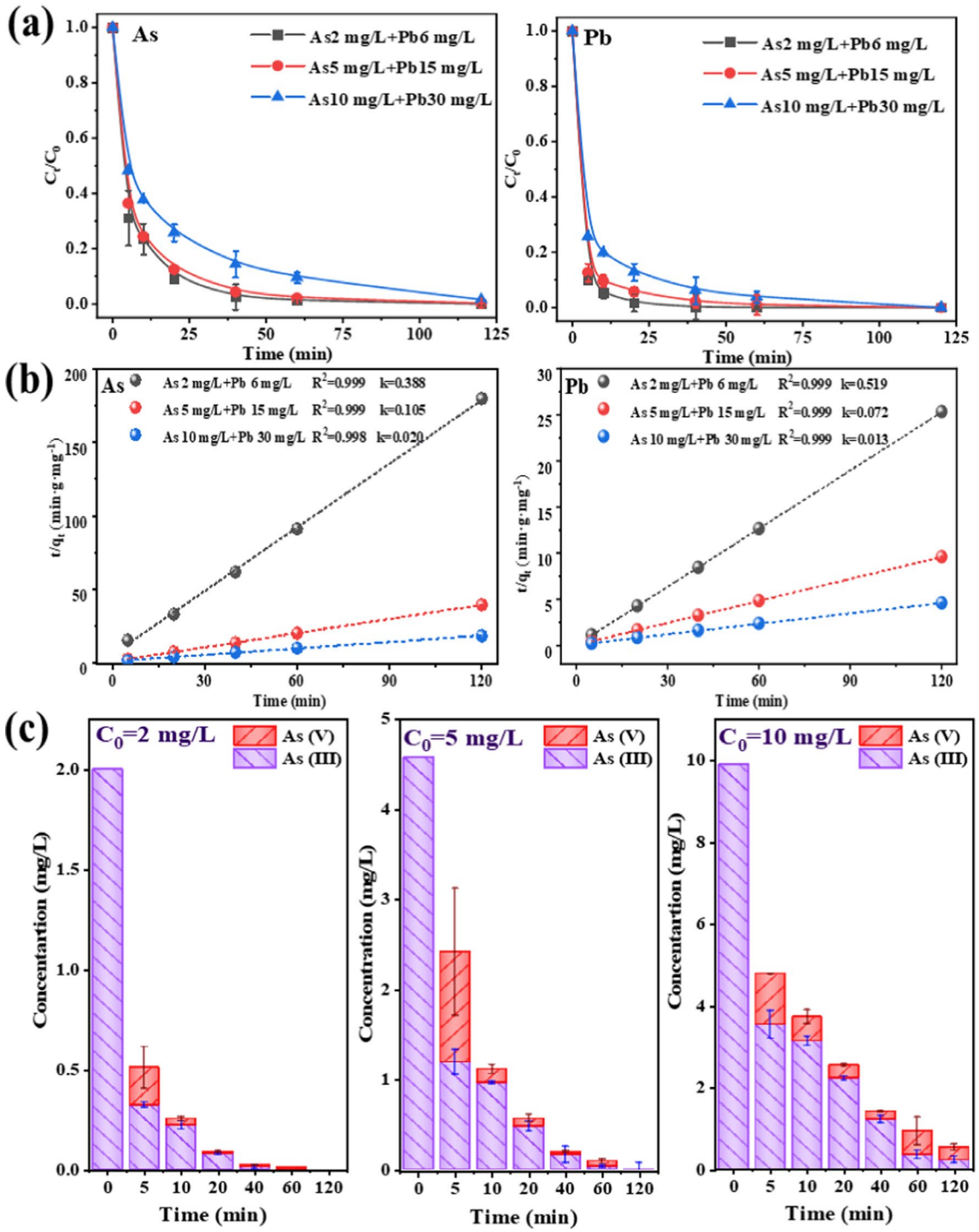

Fig. 8 Synergistic removal efficiency of As(III) and Pb(II) by NPO-NFMO with different initial concentrations of As(III) and Pb(II) (**a**), pseudo-second-order kinetic model analysis (**b**), and variation in the residual concentration of As(III) and As(V) ($^{-}$). Reaction conditions: [As(III)] = 2, 5, and 10 mg L^{-1}, [Pb(II)] = 6, 15, and 30 mg L^{-1}, 1NPO-4NFMO-based composite dosage of 1.5 g L^{-1}, V = 100 mL

the XRD pattern changed after the reaction, and the major crystal planes of $PbAs_2O_6$ and $PbFe_2(AsO_4)_2(OH)_2$ were in a good agreement with JCPDS No. 44–0427 and JCPDS No. 39–1355, which may be formed after the reaction of dissolved phosphorus, Pb^{2+}, and oxidized As(III) (Asri et al. 2010). After adsorption of As(III) and Pb(II), the main phase of the NPO-NFMO-based composite was transformed into $PbAs_2O_6$ and $PbFe_2(AsO_4)_2(OH)_2$, indicating that it was a

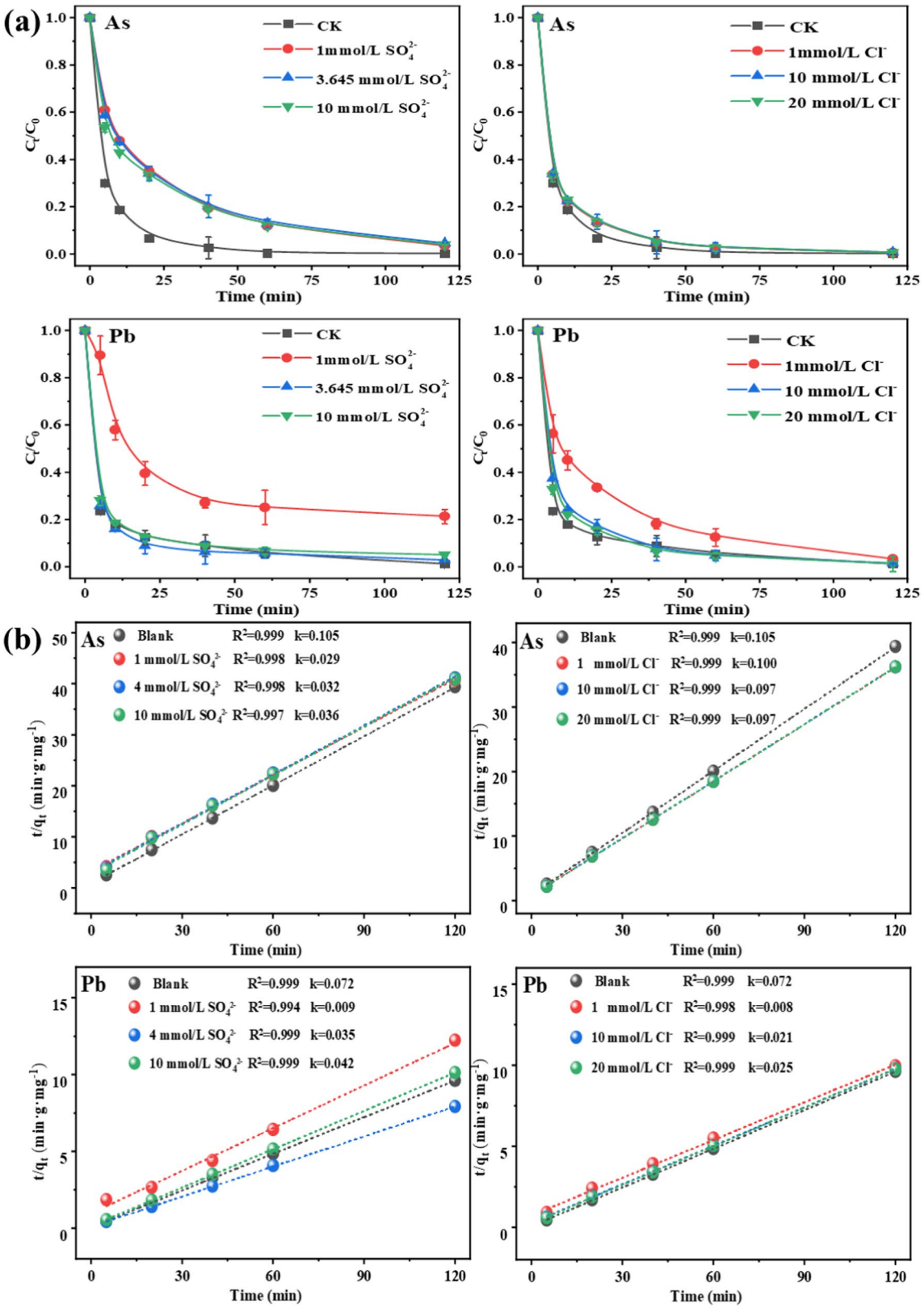

Fig. 9 Synergistic removal efficiency of As(III) and Pb(II) by NPO-NFMO with co-existing anions in groundwater (**a**), pseudo-second order kinetic model analysis (**b**). Reaction conditions: [As(III)] = 5 mg L^{-1}, [Pb(II)] = 15 mg L^{-1}, [SO_4^{2-}] = 1, 4, and 10 mmol/L, [Cl^-] = 1, 10, and 20 mmol/L, 1NPO-4NFMO-based composite dosage of 1.5 g L^{-1}, V = 100 mL

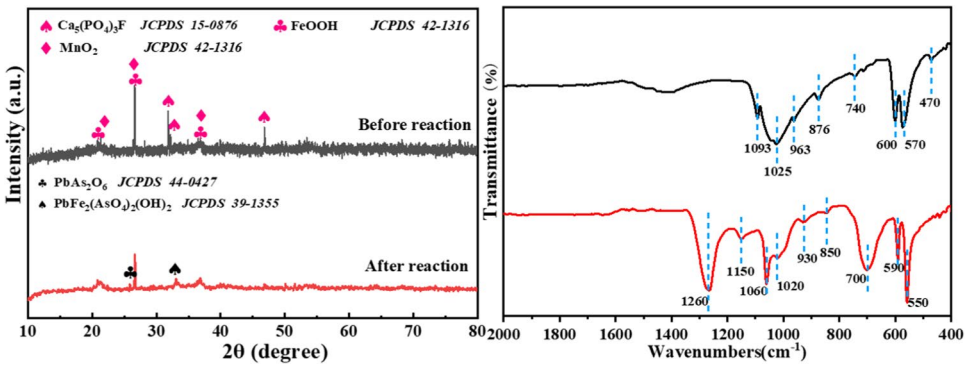

Fig. 10 XRD patterns (**a**) and FT-IR spectroscopies of the NPO-NFMO before and after reaction (**b**)

co-oxidation-precipitation-adsorption process. Figure 10b showed the FT-IR spectroscopies of the NPO-NFMO-based composite before reaction. The P-O symmetric and asymmetric stretching vibrations occur in the 963–1093 cm^{-1} spectral region as a broad peak, whereas the asymmetric P-O bending vibration gives rise to sharp peaks in 570–600 cm^{-1} region. The peaks of the pristine NPO-NFMO-based composite at 470 cm^{-1} was mainly contribution to low crystalline ferrihydrite or amorphous iron(III)-hydroxide. The FT-IR spectra of the NPO-NFMO-based composite particles after use in Fig. 10b showed enhanced signals at 1260 cm^{-1} (the asymmetric stretching vibration of P = O bond), 1150 cm^{-1} (assigned to acid phosphate (HPO_4^{2-})), 1060 cm^{-1} (symmetric and asymmetric stretching vibrations of P-O bond), 930 cm^{-1} (asymmetric stretching vibration of As-O bond) (Depalma et al. 2008), 850 cm^{-1} (As-O stretching vibration of the As-O-Fe coordination of ferric arsenate precipitate on ferrihydrite) (Jia et al. 2007), and 700 cm^{-1} (As-O stretching vibration bands of the protonated adsorbed arsenate species on ferrihydrite). The results of FT-IR were basically consistent with those of XRD. After adsorbing As and Pb, new peaks appearing at 1260 and 850 cm^{-1} were caused by the reaction of As and Pb with P-O and Fe–O functional groups on the NPO-NFMO-based composite, respectively. The transfer and disappearance of some functional groups indicated that the corresponding functional groups were involved in the removal of heavy metals to some extent.

It was noted that the weak As-O–H band at 700 cm^{-1} was shown at acidic pH indicating the present of protonated adsorbed arsenate species on ferrihydrite at acidic pH (Jia et al. 2007). The presence of a new peak at 850 cm^{-1} for both As(III)- and As(V)-laden the NPO-NFMO-based composite. It was evident that As(III) was first oxidized to As(V) and then adsorbed onto the surface of the NPO-NFMO-based composite, which was consistent with the results by Pena et al. (2006). They also compared FT-IR bands for sorbed and dissolved arsenate species, noted a marked shift in the band positions of arsenate upon sorption. For dissolved H_2AsO_4, two peaks were observed at 878 and 909 cm^{-1} corresponding to the symmetric and asymmetric stretching vibrations of As-O bonds. Upon adsorption, the peaks were shifted to 808 and 830 cm^{-1}, respectively. The shift on band positions was attributed to symmetry reduction resulting from inner-sphere complex formation. The immobilization of As was probably attributed to the interactions between the surface groups of iron oxide and arsenate by forming Fe-As complexes or the insoluble secondary minerals, such as $FeAsO_4$ and $PbFeAsO_4OH$ (He et al. 2022). Goldberg and Johnston (2001) reported that for arsenate sorbed on amorphous iron oxide, there existed two distinct bands corresponding to surface-complexed and non-surface-complexed As-O groups, respectively. In our case, however, only one single band was observed and the wavenumber was shifted to 850 cm^{-1}, indicating that surface complexation was the predominant mechanism for arsenate sorption to the NPO-NFMO composite. The peak (1150 cm^{-1}) of the used NPO-NFMO composite could be assigned to the bending vibration of hydroxyl groups of acid phosphate. Zhang et al. (2005) ascribed this phenomenon to ion exchange reaction between -OH and arsenate anions.

Figure 11 revealed that the morphology of the NPO-NFMO-based composite particles showed visible change, suggesting the reaction of the NPO-NFMO-based composite with As(III) and Pb(II). Figure 11 also depicts that the adsorbed NPO-NFMO-based composite was covered with As, Pb, Fe, Mn, P, and Ca, confirming that As and Pb were successfully encapsulated onto the NPO-NFMO-based composite. During the adsorption of Pb(II) by NPO-NFMO, the release of Ca^{2+} and a very small amount of phosphorus were also detected, indicating that an isomorphous replacement reaction might be the mechanism for Pb(II) immobilization. Meanwhile, the distribution of As and Pb might be strongly associated with Fe, P, and O, which was mainly attributed to the occurrence of Fe–O-As, Fe–O-Pb, and Fe–O-As-Pb complexation and coprecipitation on the NPO-NFMO-based composite surface.

The XPS spectra of the pristine NPO-NFMO-based composite and the NPO-NFMO-based composite after reaction in the region of Fe 2p and Mn 2p are given in Fig. 12(a, b). As can be observed, the binding energy at 711.1 eV and 642.5 eV in pristine NPO-NFMO-based composite was assigned to Fe

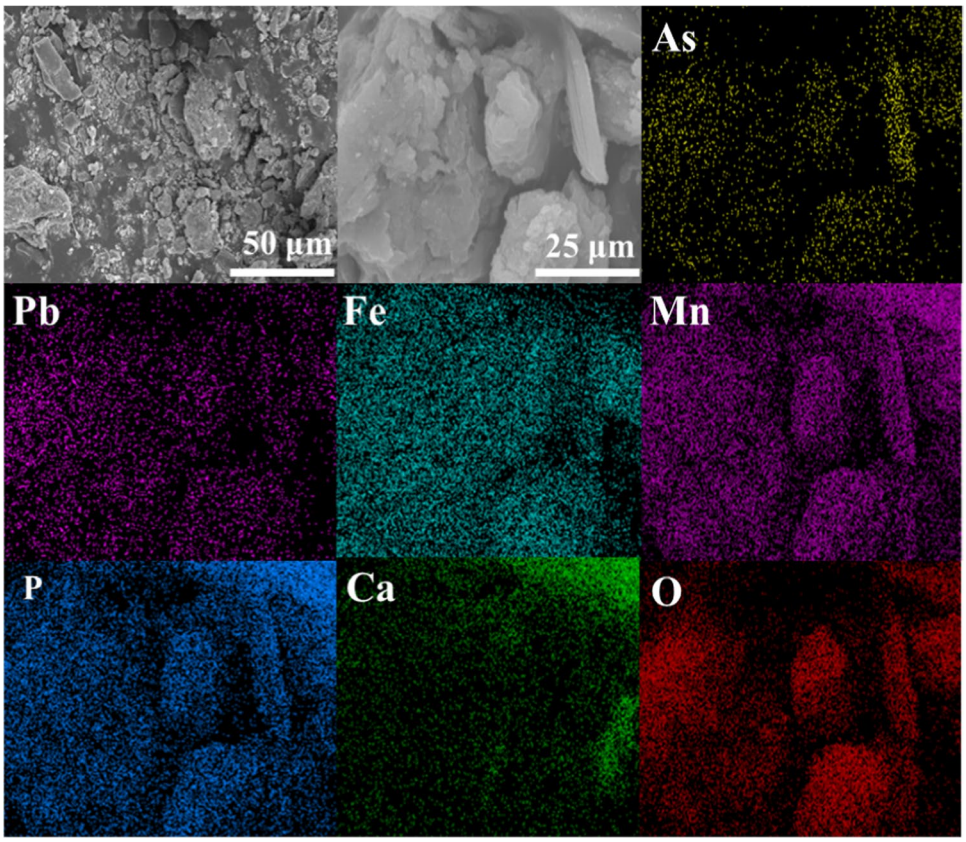

Fig. 11 SEM images and EDS-mapping of the NPO-NFMO after reaction

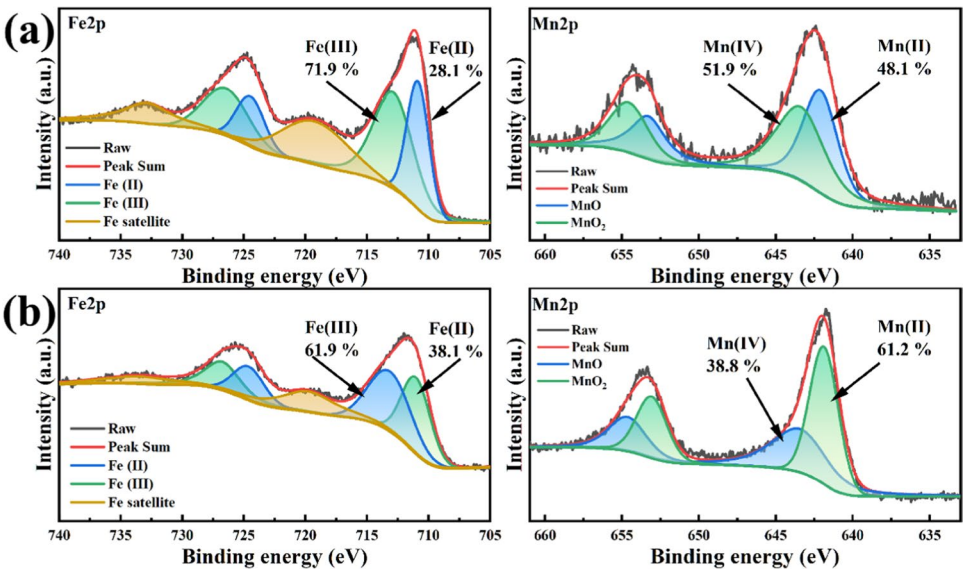

Fig. 12 XPS spectra of **a** the pristine NPO-NFMO-based composite and **b** the NPO-NFMO-based composite after reaction in the region of Fe 2p and Mn 2p

2p3/2 and Mn 2p3/2, respectively. Comparing the binding energy of the Fe2p3/2 and Mn2p3/2 before and after As(III) and Pb(II) adsorption, slight changes was observed, indicating the formation of Fe/Mn-OPb and Fe/Mn-OAs from Fe/Mn-OH. The Fe 2p3/2 profiles for the NPO-NFMO-based composite before and after reaction were deconvoluted into two Fe 2p3/2 peaks at 710.8 eV and 713.0 eV, corresponding to Fe(II) and Fe(III) with atom ratio of 28.1% and 71.9% before reaction and 38.1% and 61.9% after reaction, respectively. This observation mean that Fe(II)/Fe(III) both existed in the pristine NPO-NFMO-based composite. After the reaction, the relative content of Fe(III) on the surface decreased from ~ 71.9 to ~ 61.9%, indicating that surface iron atoms are the potential active sites. After adsorption of As(III) and Pb(II), the binding energy of

Mn 2p3/2 spectra decreased from 642.4 to 641.7 eV. This may be explained by an increase in the fraction of reduced Mn species relative to Mn(IV) originating from As(III) oxidation by Mn oxide, suggesting that Mn species mainly respond to oxidation of As(III), rather than adsorption in this case. In addition, corresponding to the total XPS spectrum after adsorption (Fig. S7), the energy spectrum of As3d could be found at 64 eV. The Mn 2p3/2 profiles for the NPO-NFMO-based composite before and after reaction were decomposed into two Mn 2p3/2 peaks at 642.2 eV and 643.6 eV, corresponding to Mn(II) and Mn(IV) with the atom ratio of 48.1% and 51.9% before reaction and 61.2% and 38.8% after reaction, respectively. Obviously, it was found that the atom ratio of Mn(IV) decreased from 51.9 to 38.8% after reaction. Consequently, the redox reaction among Mn(II) and Mn(IV) occurred on the surface of the NPO-NFMO-based composite.

Therefore, based on the above analysis, we concluded that the synergistic adsorption mechanism for the NPO-NFMO-based composite under the As-Pb co-existence system was electrostatic adsorption, oxidation, complexation, and coprecipitation. Schematic illustration of the mechanisms for simultaneous removal of As(III) and Pb(II) by the NPO-NFMO based composite was shown in Fig. 13. The involved reaction equations might be involved:

$$Ca_5(PO_4)_3F + 6H^+ \rightarrow 5Ca^{2+} + 3H_2PO_4^- + F^- \quad (4)$$

$$5Pb^{2+} + 3H_2PO_4^- + F^- \rightarrow Pb_5(PO_4)_3F + 6H^+ \quad (5)$$

$$MnO_2 + H_2AsO_3^- + 2H^+ \rightarrow Mn^{2+} + H_2AsO_4^- + H_2O \quad (6)$$

$$FeOOH + H_2AsO_4^- + H^+ \rightarrow FeAsO_4 + 2H_2O \quad (7)$$

$$3Pb^{2+} + 2H_2AsO_4^- \rightarrow Pb_3(AsO_4)_2F + 4H^+ \quad (8)$$

$$FeAsO_4 + Pb(OH)^+ + OH^- \rightarrow PbFe_2(AsO_4)_2(OH)_2 \quad (9)$$

Conclusions

A novel natural phosphorus-ferromanganese ore (NPO-NFMO) based composites were first prepared, characterized, and applied in the simultaneous remediation of arsenic- and lead-co-contaminated groundwater. Results showed that NPO-NFMO displayed highly effective adsorption performance of As(III) and Pb(II) with the maximum adsorption capacity of 6.8 mg g^{-1} and 26.5 mg g^{-1}, respectively, which was much higher than single NPO (1.7 and 7.8 mg g^{-1}) and NFMO (2.9 and 5.1 mg g^{-1}). The results suggested that the synergistic effect between NPO and NFMO enhanced the removal efficiency of As(III) and Pb(II). The adsorption kinetics of As(III) and Pb(II) on NPO-NFMO-based composites were well-described by pseudo-second-order model, indicating that the adsorption was controlled by chemisorption. The XRD, FT-IR, SEM, and XPS analyses indicated that NPO-NFMO can form stable minerals of $PbAs_2O_6$ and $PbFe_2(AsO_4)_2(OH)_2$ with Pb and As. The adsorption mechanism indicated that As(III) and Pb(II) removal might include electrostatic adsorption, oxidation, complexation, and co-precipitation. For efficiency, simplicity, and cost-effectiveness, the newly designed NPO-NFMO-based composites can be deemed as a promising amendment for simultaneous immobilization of As(III) and Pb(II) in co-contaminated soil and groundwater.

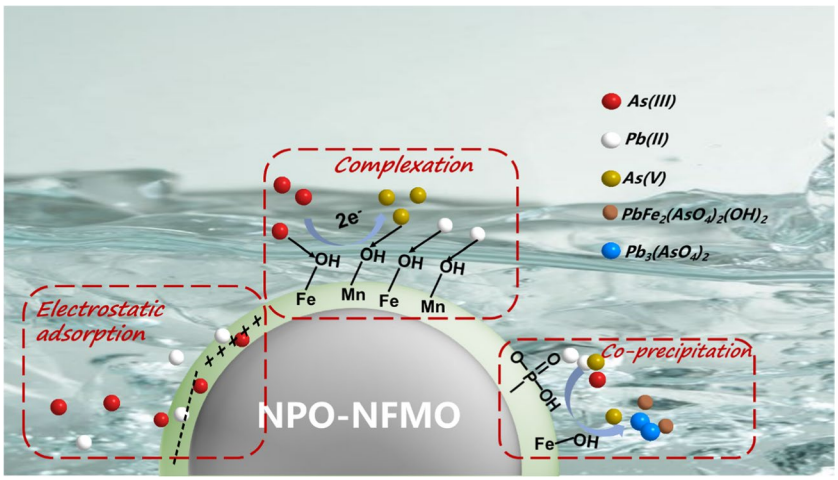

Fig. 13 Schematic illustration of the mechanisms for simultaneous removal of As(III) and Pb(II) by the NPO-NFMO-based composite

Supplementary Information The online version contains supplementary material available at https://doi.org/10.1007/s11356-023-29475-9.

Author contribution Hongli Lu: performing experiments, data analysis and processing. Xiangjian Xu: funding acquisition, resources and supervision. Yu Yang: funding acquisition, resources and supervision. Fu Xia: performing experiments, data analysis and processing. Xu Han: writing—review and editing. Han Xiao: writing—review and editing. Yonghai Jiang: funding acquisition, resources and supervision. Sheng Deng: writing—review and editing. Shuxuan Wu: data analysis and processing. Xingang Wang: performing experiments, data analysis and processing. Qinghua Yan: Resources and supervision.

Funding This research has been financially supported by the National Key Research and Development Program "Soil Pollution and Control Technology from the Ministry of Science and Technology of China" (Grant No. 2020YFC1808000 and 2019YFC1806200).

Data availability The datasets used and/or analyzed during the current study are available from the corresponding author on reasonable request.

Declarations

Ethical approval and consent to participate Not applicable.

Consent to publish Not applicable.

Competing interests The authors declare no competing interests.

References

Ain QU, Zhang H, Yaseen M et al (2020) Facile fabrication of hydroxyapatite-magnetite-bentonite composite for efficient adsorption of Pb(II), Cd(II), and crystal violet from aqueous solution. J Clean Prod 247:119088

Akin I, Arslan G, Tor A, Ersoz M et al (2012) Arsenic(V) removal from underground water by magnetic nanoparticles synthesized from waste red mud. J Hazard Mater 235–236:62–68

Asri SE, Laghzizil A, Coradin T et al (2010) Conversion of natural phosphate rock into mesoporous hydroxyapatite for heavy metals removal from aqueous solution. Colloids Surf A Physicochem Eng Asp 362(1):33–38

Bhaumik M, Maity A, Brink (2021) Zero valent nickel nanoparticles decorated polyaniline nanotubes for the efficient removal of Pb(II) from aqueous solution: Synthesis, characterization and mechanism investigation. Chem Eng J 417:127910

Bhowmick S, Chakraborty S, Mondal P et al (2014) Montmorillonite-supported nanoscale zero-valent iron for removal of arsenic from aqueous solution: Kinetics and mechanism. Chem Eng J 243:14–23

Chen J, Wang J, Zhang G et al (2018) Facile fabrication of nanostructured cerium-manganese binary oxide for enhanced arsenite removal from water. Chem Eng J 334:1518–1526

Cheng Z, Fu F, Dionysiou D et al (2016) Adsorption, oxidation, and reduction behavior of arsenic in the removal of aqueous As(III) by mesoporous Fe/Al bimetallic particles. Water Res 96:22–31

Cui H, Dong T, Hu L et al (2022) Adsorption and immobilization of soil lead by two phosphate-based biochars and phosphorus release risk assessment. Sci Total Environ 824:153957

Depalma S, Cowen S, Hoang T et al (2008) Adsorption thermodynamics of p-Arsanilic acid on iron (oxyhydr) oxides: in-situ ATR-FTIR studies. Environ Sci Technol 42(6):1922–1927

Feng W, Liu G, Wang P et al (2020) Template synthesis of a heterostructured MnO_2@SnO_2 hollow sphere composite for high asymmetric supercapacitor performance. ACS Appl Energy Mater 3(8):7284–7293

Gao J, Wang W, Rondinone AJ et al (2015) Degradation of trichloroethene with a novel ball milled Fe-C nanocomposite. J Hazard Mater 300:443–450

Goldberg S, Johnston CT (2001) Mechanisms of arsenic adsorption on amorphous oxides evaluated using macroscopic measurements, vibrational spectroscopy, and surface complexation modeling. J Colloid Interface Sci 234(1):204–216

Guan X, Dong H, Ma J et al (2009) Removal of arsenic from water: effects of competing anions on As (III) removal in $KMnO_4$-Fe(II) process. Water Res 43(15):3891–3899

Gude JCJ, Rietveld LC, Van Halem D (2017) As(III) oxidation by MnO_2 during groundwater treatment. Water Res 111:41–51

He Y, Fang T, Wang J et al (2022) Insight into the stabilization mechanism and long-term effect on As, Cd, and Pb in soil using zeolite-supported nanoscale zero-valent iron. J Clean Prod 355:131634

Hu J, Li S, Chu J et al (2019) Understanding the phase-induced electrocatalytic oxygen evolution reaction activity on FeOOH nanostructures. ACS Catal 9(12):10705–10711

Jain CK, Ali I (2000) Arsenic: occurrence, toxicity and speciation techniques. Water Res 34(17):4304–4312

Jia Y, Xu L, Wang X (2007) Infrared spectroscopic and X-ray diffraction characterization of the nature of adsorbed arsenate on ferrihydrite. Geochim Cosmochim Acta 71(7):1643–1654

Lenoble V, Laclautre C, Serpaud B et al (2004) As(V) retention and As(III) simultaneous oxidation and removal on a MnO_2-loaded polystyrene resin. Sci Total Environ 326(1):197–207

Li S, Yan W, Zhang WX (2009) Solvent-free production of nanoscale zero-valent iron (nZVI) with precision milling. Green Chem 11(10):1618–1626

Liao J, Xiong T, Ding L et al (2022) Design of a renewable hydroxyapatite-biocarbon composite for the removal of uranium (VI) with high-efficiency adsorption performance. BCHA 4(1):1–18

Ma QY, Logan TJ, Traina SJ et al (1994) Effects of NO_3^-, Cl^-, F^-, SO_4^{2-}, and CO_3^{2-} on Pb^{2+} immobilization by hydroxyapatite. Environ Sci Technol 28(3):408–418

Meng K, Wu X, Zhang X et al (2019) Efficient adsorption of the Cd(II) and As(V) using novel adsorbent ferrihydrite/manganese dioxide composites. ACS Omega 4(20):18627–18636

Pena M, Meng X, Korfiatis GP et al (2006) Adsorption mechanism of arsenic on nanocrystalline titanium dioxide. Environ Sci Technol 40(4):1257–1262

Qureshi SS, Memon SA, Ram N et al (2022) Rapid adsorption of selenium removal using iron manganese-based micro adsorbent. Sci Rep 12(1):1–13

Shi K, Radhakrishnan M, Dai X et al (2021) NemA catalyzes trivalent organoarsenical oxidation and is regulated by the trivalent organoarsenical-selective transcriptional repressor NemR. Environ Sci Technol 55(9):6485–6494

Stumm W, Morgan J (1996) Aquatic chemistry. In: Chemical equilibria and rates in natural waters 3rd edn. New York: Wiley-Interscience, p 462–466

Sun Y, Yu IKM, Tsang DCW et al (2019) Multifunctional iron-biochar composites for the removal of potentially toxic elements, inherent cations, and hetero-chloride from hydraulic fracturing wastewater. Environ Int 124:521–532

Wang L, Cho DW, Tsang DCW et al (2019) Green remediation of As and Pb contaminated soil using cement-free clay-based stabilization/solidification. Environ Int 126:336–345

Wang YN, Tsang YF, Wang H et al (2020) Effective stabilization of arsenic in contaminated soils with biogenic manganese oxide (BMO) materials. Environ Pollut 258:113481

Wang H, Chen Q, Liu R et al (2022) Synthesis and application of starch-stablized Fe-Mn/biochar composites for the removal of lead from water and soil. Chemosphere 305:135494

Xia Q, Lamb D, Peng C et al (2017) Interaction effects of As, Cd and Pb on their respective bioaccessibility with time in co-contaminated soils assessed by the Unified BARGE Method. Environ Sci Pollut Res 24(6):5585–5594

Zhang Y, Yang M, Dou XM et al (2005) Arsenate adsorption on an Fe-Ce bimetal oxide adsorbent: role of surface properties. Environ Sci Technol 39(18):7246–7253

Zhang G, Qu J, Liu H et al (2007) Preparation and evaluation of a novel Fe-Mn binary oxide adsorbent for effective arsenite removal. Water Res 41(9):1921–1928

Zhang L, Fu Z, Wu Z et al (2014) Investigation of structural and luminescent properties of Ce^{3+}/Mn^{2+} ions-doped $Ca_5(PO_4)_3F$. Mater Res Bull 56:65–70

Zhang G, Liu Y, Wang J et al (2020) Efficient arsenic(III) removal from aqueous solution by a novel nanostructured iron-copper-manganese trimetal oxide. J Mol Liq 309:112993